

Cross-correlating galaxies and cosmic dispersion measures: Constraints on the gas-to-halo mass relation from 2MASS galaxies and 133 localized fast radio bursts

Masato SHIRASAKI^{1,2,*}, Ryuichi TAKAHASHI³, Ken OSATO⁴⁻⁶, and Kunihito IOKA⁷

¹National Astronomical Observatory of Japan (NAOJ), National Institutes of Natural Sciences, Tokyo 181-8588, Japan

²The Institute of Statistical Mathematics, Tokyo 190-8562, Japan

³Faculty of Science and Technology, Hirosaki University, Aomori 036-8560, Japan

⁴Center for Frontier Science, Chiba University, Chiba 263-8522, Japan

⁵Department of Physics, Graduate School of Science, Chiba University, Chiba 263-8522, Japan

⁶Kavli Institute for the Physics and Mathematics of the Universe (WPI), The University of Tokyo Institutes for Advanced Study, The University of Tokyo, Chiba 277-8583, Japan

⁷Yukawa Institute for Theoretical Physics, Kyoto University, Kyoto 606-8502, Japan

*E-mail: masato.shirasaki@nao.ac.jp

Abstract

We conduct a cross-correlation analysis between large-scale structures traced by the Two Micron All Sky Survey (2MASS) galaxy catalog and the cosmic dispersion measures of 133 localized fast radio bursts (FRBs). The cross-correlation signal is measured as a function of the comoving separation R between 2MASS galaxies and background FRB sightlines, making full use of the available redshift information for both datasets. Our measurements are consistent with a null detection over the range $0.01 < R [h^{-1} \text{Mpc}] < 1$. Using a halo-based model in which free-electron density profiles are drawn from the hydrodynamical simulation IllustrisTNG-300 (TNG300), we show that the null signal at $R \sim 0.01 h^{-1} \text{Mpc}$ is inconsistent with the TNG300 prediction. This discrepancy indicates that the hot-gas mass fraction in halos with masses of $10^{12-13} M_\odot$ hosting 2MASS galaxies must be lower than that predicted by TNG300. A simple phenomenological modification of the TNG300 model suggests that the hot-gas mass fraction in halos of $10^{12-13} M_\odot$ should be below $\sim 10\%$ of the global baryon fraction in the nearby universe, implying the need for stronger feedback in this mass range. Our constraints are consistent with those inferred from X-ray emission and Sunyaev-Zel'dovich measurements in galaxies, while providing a direct estimate of the hot-gas mass fraction that does not rely on electron-temperature measurements. These results demonstrate that galaxy-FRB cross correlations offer a powerful probe of feedback processes in galaxy formation.

Keywords: methods: statistical — intergalactic medium — large-scale structure of universe

1 Introduction

Fast radio bursts (FRBs) are radio transients with their typical pulse duration being several milliseconds (see Petroff et al. 2019 for a review). Although their physical origin is yet unclear (Zhang 2023), FRBs have attracted much attention as a next-generation probe of cosmology. The arrival time of FRB pulses is known to be dispersed due to light propagation through intervening electron plasma. The frequency dependence in the arrival time t_{arr} is written as

$$t_{\text{arr}}(\nu) = \frac{e^2}{2\pi m_e c} \frac{\text{DM}}{\nu^2} = 4.14 \text{ ms} \left(\frac{\text{DM}}{\text{pc/cc}} \right) \left(\frac{\nu}{\text{1GHz}} \right)^{-2}, \quad (1)$$

where e is the electron charge, m_e is the electron mass, c is the speed of light, ν is the observed frequency, and DM is called the dispersion measure, equaling the column density of free electrons along the line-of-sight to the source. Hence, measurements of delays in FRB-pulse arrivals provide a unique means of mapping free electrons in the universe, which is an important pillar of baryonic components in the concordance cosmological model.

Baryons are known to occupy only a $\sim 5\%$ of the energy-density budget in the present-day universe (e.g. Planck Collaboration et al. 2020), but their feedback plays an essential role in shaping our ob-

servable universe. For instance, stellar winds and supernovae explosions can regulate star-forming processes across galactic scales (e.g. Dekel & Silk 1986), while active galactic nuclei are an important contributor to foundation of scaling relations in galaxy clusters (e.g. Eckert et al. 2021) as well as termination of star formations at massive galaxies (e.g. Fabian 2012). Furthermore, modern cosmology faces a major challenge in quantifying the baryonic feedback and its impact on statistical analyses of cosmic large-scale structures as precise datasets become available (Chisari et al. 2019).

Current understanding of baryonic feedback in large-scale structures remains limited. A series of Stage-III galaxy imaging surveys has demonstrated precise estimation of cosmological parameters using weak lensing effects caused by low-redshift ($z \sim 0.5-2$) matter distributions alone (e.g. Asgari et al. 2021; Amon et al. 2022; Secco et al. 2022; Dalal et al. 2023; Li et al. 2023). However, the accuracy of these parameter estimates depends critically on the details of baryonic feedback modeling (e.g. Amon & Efstathiou 2022; Chen et al. 2023; Aricò et al. 2023; Bigwood et al. 2024; Terasawa et al. 2025; Broxterman et al. 2025).

Hydrodynamical simulations covering cosmological volumes are among the most essential approaches for predicting baryonic

feedback effects in large-scale structures. Despite their success, these simulations face a fundamental challenge in spatial resolution: it is impractical to capture the enormous dynamic range of relevant physical scales, from sub-pc to $O(1)$ Gpc, within a single simulation. A common practice is to introduce subgrid recipes to reduce computational costs in the highest-density environments (e.g. Valentini & Dolag 2025 for a review). However, this phenomenological methodology must be validated against multiple observations.

Most cosmological hydrodynamical simulations calibrate their subgrid recipes using observations of stellar components across a wide range of redshifts, as well as intracluster media at low redshifts. Observational information about gaseous matter in and around galaxy-sized objects is highly sought to further improve the realism of these simulations. In this context, statistical analyses using large samples of FRBs have been proposed as a way to overcome current limitations, offering valuable insights into baryonic feedback effects. These include one-point probability functions of dispersion measures (Medlock et al. 2024; Zhang et al. 2025; Sharma et al. 2025b; Guo & Lee 2025; Medlock et al. 2025; Reischke & Hagstotz 2025), autocorrelation functions of FRB dispersion measures (Takahashi et al. 2021; Nicola et al. 2022), cross-correlation functions with tracers of large-scale structures (Shirasaki et al. 2022; Reischke et al. 2023; Hussaini et al. 2025; Wang et al. 2025; Leung et al. 2025; Takahashi et al. 2025), and various combinations of these approaches (Shirasaki et al. 2017a; Sharma et al. 2025a).

In this paper, we perform a cross-correlation analysis between a galaxy catalog with spectroscopic redshift information and 133 localized FRBs. Our FRB sample is introduced in the companion paper (Takahashi et al. 2025), which compiles publicly available FRBs with precise localizations. We propose a novel estimator for real-space cross correlations, incorporating a robust background selection based on redshifts. This estimator is designed to be free from contamination by Galactic and FRB-host dispersion measures, providing a clean probe of the free-electron density at the redshifts of foreground galaxies. Our measurements can be readily interpreted using a standard halo-based modeling framework (Cooray & Sheth 2002), widely adopted in studies of large-scale structure. Using well-defined cross-correlation measurements and an efficient modeling approach, we aim to place independent constraints on gas-to-halo mass relations in the local universe at a redshift of $z \sim 0.03$.

It is worth noting that Hussaini et al. (2025) also conducted a similar cross-correlation analysis, but there are notable differences between the two studies. We use spectroscopic galaxy redshifts for accurate measurements, whereas Hussaini et al. (2025) relied on multiple galaxy catalogs with photometric redshifts. Their analysis is based on 61 localized FRBs, but their foreground galaxy sample is larger than ours. We pay particular attention to measuring cross correlations at scales down to ~ 0.01 Mpc, as small-scale information is crucial for constraining baryonic physics in group-sized objects – an aspect not addressed in Hussaini et al. (2025). We expect that the photometric-redshift uncertainties of their foreground galaxy sample limit their ability to probe such small scales in Hussaini et al. (2025).

The remainder of this paper is organized as follows: Section 2 describes the dataset used for the cross-correlation measurements. Section 3 summarizes our estimator and the methodology for assessing statistical and systematic uncertainties. Section 4 introduces the halo-model framework used to generate predictions for comparison with our measurements. Our main results are pre-

sented in Section 5, and we conclude in Section 6.

Throughout this paper, we assume a spatially flat Λ CDM cosmology with $\Omega_m = 1 - \Omega_\Lambda = 0.315$, $\Omega_b = 0.049$, $h = 0.674$, $n_s = 0.965$, and $\sigma_8 = 0.811$, consistent with recent measurements of cosmic microwave background anisotropies by the Planck satellite (Planck Collaboration et al. 2020). We adopt the spherical-overdensity mass convention, $M_\Delta = 4\pi r_\Delta^3 \rho_{\text{crit},z} \Delta / 3$, where r_Δ is the halo radius within which the mean density equals Δ times the critical density $\rho_{\text{crit},z}$ at redshift z . Unless otherwise stated, we use $M \equiv M_{200}$ as our fiducial choice. Conversions between different spherical-overdensity masses follow Hu & Kravtsov (2003).

2 Data

2.1 2MASS galaxy catalog

We use the galaxy catalog from the 2MASS Redshift Survey (2MRS; Huchra et al. 2012), a spectroscopic follow-up of the Two Micron All Sky Survey (Skrutskie et al. 2006). Ando et al. (2018) showed that the redshift distribution of 2MASS galaxies is well described by the following functional form:

$$p_{\text{2MASS}}(z) = \frac{n}{z_0 \Gamma[(m+1)/n]} \left(\frac{z}{z_0} \right)^m \exp \left[- \left(\frac{z}{z_0} \right)^m \right], \quad (2)$$

where $\Gamma(x)$ is the Gamma function, and the parameters $m = 1.31$, $n = 1.64$, and $z_0 = 0.0266$ are inferred in Ando et al. (2018). The 2MRS provides a nearly volume-limited sample up to $z \simeq 0.02$ with high redshift completeness for galaxies with $K_s \leq 11.75$. Clustering analyses in Ando et al. (2018) also constrain the halo occupation distributions (HOD) of 2MASS galaxies with good precision. We rely on their HOD model to infer typical host halo masses of 2MASS galaxies when interpreting our cross-correlation measurements. Details of the HOD are given in Section 4.

In this paper, we account for redshift completeness¹ using information from Lavaux & Hudson (2011) and the HEALPix² package (Górski et al. 2005). First, we compute the average completeness in a HEALPix map with resolution NSIDE = 32, referring to completeness at $K_s \leq 11.5$ from the catalog in Lavaux & Hudson (2011). We find that HEALPix pixels with average completeness greater than 0.5 cover about $\sim 80\%$ of the sky. Each 2MASS galaxy is then assigned a weight equal to the average completeness of its corresponding HEALPix pixel. To avoid regions near the Galactic plane in our cross-correlation analysis, we set the weight to zero for galaxies at $|b| < 5^\circ$ for $30^\circ < l < 330^\circ$ and $|b| < 10^\circ$ otherwise, where b and l denote Galactic latitude and longitude, respectively. We also generate 1000 random catalogs using the completeness map and uniform sampling of random points on a sphere. Each random catalog contains 43,533 entries, matching the actual 2MASS catalog. These random catalogs are used to subtract the mean offset of dispersion measures from our cross-correlation measurements. Additionally, we divide the galaxy catalog into 40 subregions using the dsigma³ package (Huang et al. 2022). These subregions with similar area allow us to estimate the covariance matrix of our measurements using the standard delete-one jackknife method commonly employed in galaxy analyses (Norberg et al. 2009; Shirasaki et al. 2017b; Singh et al. 2017).

The upper panel of Fig. 1 shows the redshift distribution of 2MASS galaxies, while the lower panel illustrates the large-scale

¹ This is the fraction of objects in the 2MASS photometric sample for which reliable redshift measurements have been obtained.

² <https://healpix.sourceforge.io/>

³ <https://dsigma.readthedocs.io/en/latest/index.html>

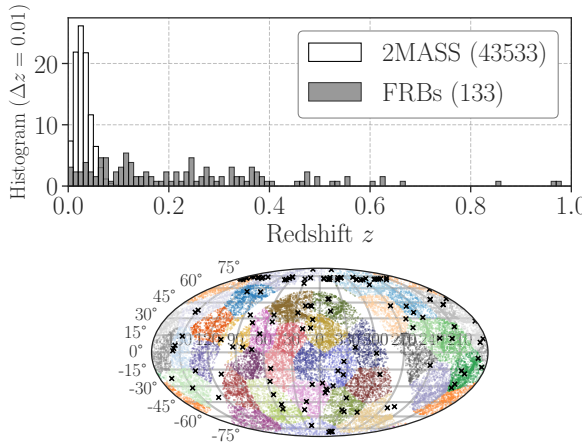


Fig. 1. Redshift and angular distributions of our dataset. The upper panel summarizes the histogram of 2MASS-galaxy and FRB redshifts with the bin width of $\Delta z = 0.01$, while colored points and black cross symbols in the lower panel represent the angular positions of 2MASS galaxies and 133 localized FRBs, respectively. We adopt the equatorial coordinate system in the lower panel. Note that the different colors in the lower panel highlight 40 jackknife subdivisions of the 2MASS galaxy catalog. Those subregions are used for the covariance estimation in our cross-correlation measurements. Alt text: Graphs and data on spatial information of galaxies and fast radio bursts.

structure traced by these galaxies across the full sky. Different colors in the lower panel indicate the subregions used for jackknife-based covariance estimation.

2.2 Localized fast radio bursts

We use the sample of localized FRBs summarized in Takahashi et al. (2025). The authors compiled 133 FRBs whose host galaxies were identified through follow-up observations reported in the literature (see Table 6 in Takahashi et al. 2025 for the full list). They then inferred the cosmic dispersion measures⁴ for individual FRBs using a likelihood analysis based on a mixture of three log-normal distributions of dispersion measures. Their likelihood analysis adopted two different models for the MW contribution (Cordes & Lazio 2002; Yao et al. 2017; Yamasaki & Totani 2020) and two different redshift evolutions for the host-galaxy component. For the redshift dependence of host-galaxy dispersion measures, the authors used a common model assuming a power-law evolution with $(1+z)^{-1}$ (Ioka 2003; Zhou et al. 2014), while also exploring a freely varying power-law index motivated by recent theoretical studies (Jaroszyński 2020; Zhang et al. 2020; Mo et al. 2023; Kovacs et al. 2024; Theis et al. 2024; Reischke et al. 2025). In the end, their inferred cosmic dispersion measures for the localized FRBs are categorized into four classes: N1, Nbeta, Y1, and Ybeta. We use these four estimates in our cross-correlation measurements to assess systematic uncertainties arising from the component separation of observed dispersion measures.

It is important to note that the FRB angular positions and redshifts in Takahashi et al. (2025) are precisely determined through follow-up observations. This accurate localization enables us to

measure the cross-correlation between cosmic dispersion measures and the large-scale structure traced by 2MASS galaxies as a function of comoving separation. Furthermore, the secure redshift estimates allow us to select background FRBs relative to individual 2MASS galaxies, eliminating potential contamination from host-galaxy dispersion measures in our cross-correlation analysis. This setup is crucial for estimating the average free-electron density profile around 2MASS galaxies alone. It is worth noting that the previous work (Hussaini et al. 2025) did not pay attention to this background selection. We describe the details of our cross-correlation measurement procedure in Section 3. The redshift distribution of the FRB sample is shown in the upper panel of Fig. 1, while crosses in the lower panel indicate the FRB locations.

3 Cross-correlation measurements

The cross-correlation function between galaxies and FRB dispersion measures is defined as

$$\xi_{\text{gd}}(R) = \langle \delta_g(\boldsymbol{\theta}_g, z_g) \text{DM}(\boldsymbol{\theta}_s, z_s) \rangle, \quad (3)$$

where $\delta_g(\boldsymbol{\theta}_g, z_g)$ is the overdensity field of the galaxy with its angular position $\boldsymbol{\theta}_g$ and redshift z_g , and $\text{DM}(\boldsymbol{\theta}_s, z_s)$ represents the dispersion measure coming from the FRB with its angular position $\boldsymbol{\theta}_s$ and redshift z_s . In Eq. (3), we define a comoving separation R by using known redshifts of galaxies as $R = \chi(z_g)\Delta\theta_{gs}$, where $\chi(z)$ is the comoving distance to redshift z and $\Delta\theta_{gs}$ is the angular separation between galaxy and FRB in each pair. This definition of ξ_{gd} is intended to measure the average free-electron density profile around the foreground galaxy sample, borrowing the concept from galaxy-galaxy lensing measurements (e.g. Mandelbaum 2015; Umetsu 2020 for reviews). When background FRBs can be securely selected relative to the galaxies based on their redshifts, the cross-correlation in Eq. (3) arises solely from the number-density perturbations of free electrons at the galaxy redshifts z_g . This enables a robust measurement of the average hot-gas mass associated with the foreground galaxies without contamination from FRB-host dispersion measures, providing valuable insights into baryonic feedback processes in the universe.

3.1 Estimator

In practice, we can estimate the cross-correlation of ξ_{gd} from a discrete set of positions and redshifts of galaxies and FRBs as

$$\hat{\xi}_{\text{gd}}(R_i) = \frac{\sum_{gs \in R_i} w_g w_s \Delta \text{DM}_s}{\sum_{gs \in R_i} w_g w_s} - (\text{signal around random})|_{R_i}, \quad (4)$$

where the summation “gs” run over all galaxy-FRB pairs that lie in the i -th radial bin $R_i \equiv \chi(z_g)\Delta\theta_{gs}$; w_g represents the weight of the g -th galaxy accounting for the redshift completeness in the 2MRS; w_s is the weight of the s -th FRB introduced to downweight the contribution from FRBs with large uncertainties in estimating MW dispersion measures; we define ΔDM_s as residual dispersion measure of the s -th FRB;

$$\Delta \text{DM}_s \equiv \text{DM}_{\text{obs},s} - \text{DM}_{\text{MW},s} - \int_0^{z_s} \frac{cdz}{H(z)} \bar{n}_e (1+z), \quad (5)$$

where $\text{DM}_{\text{obs},s}$ and $\text{DM}_{\text{MW},s}$ are the observed and MW dispersion measures for the s -th FRB, $H(z)$ is the Hubble parameter at z , and \bar{n}_e represents the mean comoving number density of free electrons. We use an estimate of \bar{n}_e inferred from the likelihood analysis in Takahashi et al. (2025), while it depends on the detail of

⁴ An observed dispersion measure can be expressed as the sum of three components: contributions from intervening large-scale structures (LSS) between the FRB and the observer, the FRB host galaxy, and the Milky Way (MW). We define the “cosmic” dispersion measure as the sum of the LSS and host-galaxy components.

component separations. Note that we impose a selection of background FRBs in the computation of Eq. (4) with $z_s \geq z_g + \Delta z$, where Δz is a parameter to minimize interlopers in our analysis. In Eq. (5), we do not subtract the FRB-host component to make our analysis insensitive to the choice of FRB models. We set $\Delta z = 0.05$ throughout this paper. Note that a more conservative choice with $\Delta z = 0.1$ does not affect our measurements (but increases the statistical errors). The weight w_s is set to an inverse variance by using the variance of MW dispersion measure on an FRB-by-FRB basis. Finally, the second term on the right-hand side of Eq. (4) denotes the signal around a set of random positions, which is measured by replacing foreground galaxies with random points. We need to subtract this random signal to evaluate an excess from a uniform contribution of dispersion measures to all radial bins.

In the measurements, we employ a logarithmic binning with 10 bins ranging from $R = 0.01 h^{-1} \text{Mpc}$ to $R = 100 h^{-1} \text{Mpc}$ for our analysis. The covariance matrix of our cross-correlation measurements is estimated with the 40 jackknife samples for our fiducial choice. For comparison, we also estimate the covariance matrix of ξ_{gd} by producing 300 realizations of ΔDM with random shuffling of dispersion measures (we randomly shuffle ΔDM_s but fix each FRB coordinate). Note that the jackknife errors include sample-variance contributions but those cannot be applied to the data at large R beyond the size of jackknife subregions. The random-shuffling errors can be used as a robust estimate of shot noises over a wide range of R . Hence, we decide to use the data for scientific analyses only when its jackknife error is greater than the random-shuffling counterpart.

Figure 2 summarizes our measurements. The top panel shows the cross-correlation functions with the jackknife errors. We have four different measurements there as four different estimates of ΔDM are available. The middle upper panel represents the ratio of the jackknife error to the random-shuffling counterpart. The gray filled region in the upper two panels highlights the data with its jackknife errors of ξ_{gd} smaller than the random-shuffling ones. To make our analysis conservative, we avoid to use the data in the gray region for comparison with theoretical models, leaving 5 bins in the range of $0.01 < R [h^{-1} \text{Mpc}] < 1$ in the end. For reference, we also show the number of pairs in each radial bin at the middle lower panel. To be specific, 339 and 2224 galaxy-FRB pairs are available at $R < 0.1 h^{-1} \text{Mpc}$ and $R < 1 h^{-1} \text{Mpc}$, respectively.

3.2 Boost factor

Although our analysis introduces the non-zero parameter Δz to ensure secure background selection, it remains possible that some FRBs are physically associated with their foreground galaxies. Misidentification of host galaxies can occur, particularly for non-repeating FRBs. Additionally, current observations may miss certain bursts if they experience significant pulse broadening due to multi-path propagation in inhomogeneous plasma (e.g. Seebeck et al. 2021; Chawla et al. 2022; Merryfield et al. 2023; Shivraj Patil et al. 2025). At face value, the top panel of Fig. 2 shows a trend of decreasing ξ_{gd} as the galaxy-FRB separation becomes smaller. This trend is consistent with the expectation that FRB pulse scattering times increase in denser environments (e.g., galactic centers; see also Cordes et al. 2016; Vedantham & Phinney 2019; Ocker et al. 2022), suggesting that our cross-correlation measurements may be affected by scattering effects.

To test whether our background selection is impacted by these possibilities, we use the ratio of the number of galaxy-FRB

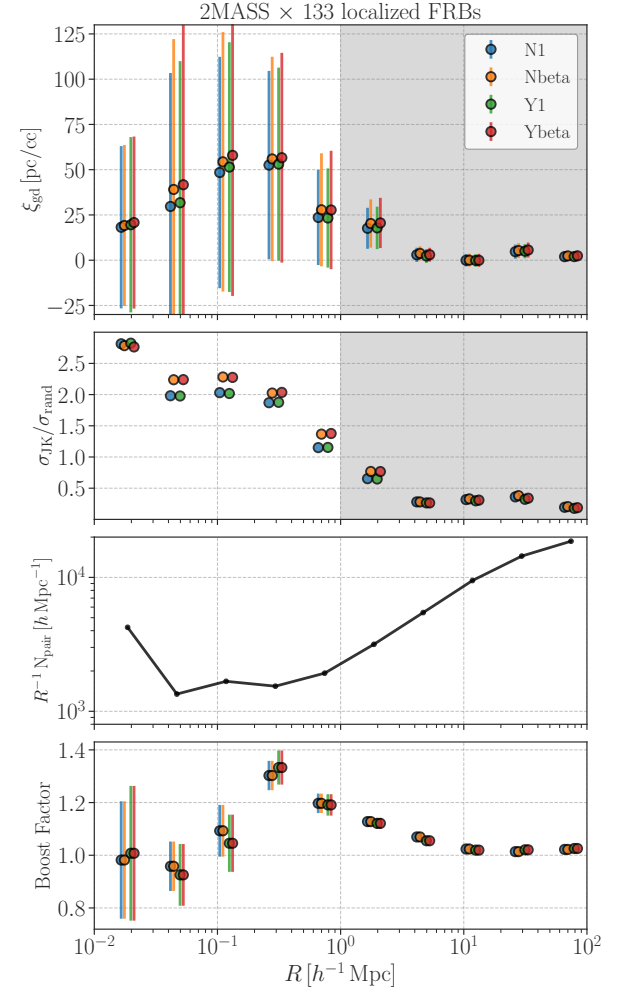


Fig. 2. A summary of our cross-correlation measurements. The top, middle upper, middle lower, and bottom panels show the cross-correlation functions between 2MASS and FRB dispersion measures, the ratio of the jackknife errors to the random-shuffling shot noises, the number of galaxy-FRB pairs at each radial bin, and the boost factor (a diagnostic quantity for secure selections of background FRBs), respectively. Different colored points in this figure highlight that our measurements rely on the four different estimates of MW dispersion measures. The gray filled regions in the top two panels represent the jackknife-based estimate of statistical errors at $R > 1 h^{-1} \text{Mpc}$ is not appropriate for scientific analyses. Note that our analysis will be subject to misidentification of background FRBs or/and observational selection effects of FRBs when the boost factor significantly deviates from unity. We describe the boost factor and its role in Section 3.2. Alt text: Graphs and data on our cross-correlation measurements.

pairs to the number of random-FRB pairs. This ratio, known as the boost factor in galaxy-galaxy lensing analyses (Hirata et al. 2004; Mandelbaum et al. 2005), allows us to assess the validity of our background selection in the cross-correlation measurements. Accounting for weights, we define the boost factor as

$$B(R_i) = \left(\sum_{gs} w_g w_s / \sum_{gs} w_g \right) / \left(\sum_{rs} w_r w_s / \sum_{rs} w_r \right), \quad (6)$$

where the summation “*gs*” and “*rs*” run over all galaxy-FRB pairs and random-FRB pairs that lie in the *i*-th radial bin R_i , respectively. Note that $B > 1$ is expected if some FRBs are physically associated with foreground galaxies, while $B < 1$ suggests that some FRBs may be missed due to scattering effects on their pulses.

The bottom panel of Fig. 2 summarizes our boost factor measurements. We estimate the errors using 300 bootstrap realizations of random catalogs. We find that boost factors at $R \lesssim 0.1 h^{-1} \text{Mpc}$ are consistent with unity, indicating that our FRB sample is unaffected by scattering effects. At $R \gtrsim 0.3 h^{-1} \text{Mpc}$, we observe a moderate deviation from unity, but this has minimal impact on our cross-correlation measurements given the large statistical uncertainties. The radius of $R = 0.3 h^{-1} \text{Mpc}$ roughly corresponds to 0.1 degrees for the median redshift of the 2MASS galaxies, probably relating to localization errors in current FRB observations. We therefore conclude that our background selection is sufficiently robust for the cross-correlation analysis at this stage.

3.3 Statistical significance

The detection significance of the cross correlation function is characterized as the signal-to-noise ratio, which is defined by

$$(\text{S}/\text{N})^2 = \sum_{ij} \hat{\xi}_{\text{gd}}(R_i) \text{Cov}_{ij}^{-1} \hat{\xi}_{\text{gd}}(R_j), \quad (7)$$

where $\hat{\xi}_{\text{gd}}(R_i)$ represents the cross correlation function at the *i*-th radial bin as measured in Eq. (4) and Cov is the jackknife covariance matrix for our measurements. In the range of $0.01 < R [h^{-1} \text{Mpc}] < 1$, we find that $(\text{S}/\text{N})^2 = 9.44, 8.44, 11.8$, and 10.4 for the estimates with N1, Nbeta, Y1, and Ybeta, respectively⁵. Since we have 5 degrees of freedom in our measurements, those values of $(\text{S}/\text{N})^2$ are consistent with a null detection at a 97% confidence level. For the sake of completeness, we provide numerical values of $\hat{\xi}_{\text{gd}}(R_i)$ and its covariance matrix in Appendix 1.

4 Model

We here describe a theoretical model to be compared with our measurements. The angular number density of foreground galaxies can be decomposed into

$$n_g(\boldsymbol{\theta}_g) = \bar{n}_g [1 + \delta_g(\boldsymbol{\theta}_g)], \quad (8)$$

where \bar{n}_g is the average angular number density and it is also computed as

$$\bar{n}_g = \int dz p(z) \frac{d\chi}{dz} \chi^2 \bar{n}_{g,3D}(z), \quad (9)$$

where $p(z)$ is the selection function of galaxies in redshifts (given by Eq. (2) in our case), and we introduce $\bar{n}_{g,3D}(z)$ to be the three-dimensional average number density of the galaxies at redshift z in the comoving frame. The overdensity field δ_g is then written in terms of its three-dimensional counterpart as

⁵ The corresponding *p*-values are computed as 0.092, 0.13, 0.037, and 0.064 for 5 degrees of freedom.

$$\delta_g(\boldsymbol{\theta}_g) = \frac{1}{\bar{n}_g} \int dz p(z) \frac{d\chi}{dz} \chi^2 \bar{n}_{g,3D}(z) \delta_{g,3D}(\mathbf{x}). \quad (10)$$

Here we denote the three-dimensional overdensity field as $\delta_{g,3D}(\mathbf{x})$ at the position of $\mathbf{x} = (\chi, \boldsymbol{\theta})$.

Dispersion measures from intervening plasma between sources at redshift z_s and an observer are formally computed as

$$\text{DM}(\boldsymbol{\theta}_s, z_s) = \int_0^{z_s} d\chi (1 + z[\chi]) n_e(\chi, \boldsymbol{\theta}_s), \quad (11)$$

where n_e represents the comoving number density of free electrons. Suppose we can surely select the background sources with redshift information, the cross correlation function can be computed as (e.g. Shirasaki et al. 2022)

$$\xi_{\text{gd}}(R) = \frac{1}{\bar{n}_g} \int dz p(z) \frac{d\chi}{dz} \chi^2 (1 + z) \bar{n}_{g,3D}(z) \times \int \frac{k dk}{2\pi} P_{\text{gd}}(k; \chi) J_0(kR), \quad (12)$$

$$P_{\text{gd}}(k; \chi) \equiv \int d^3 r \langle \delta_{g,3D}(\mathbf{x}) n_e(\mathbf{x} + \mathbf{r}) \rangle|_\chi \exp(-\mathbf{k} \cdot \mathbf{r}), \quad (13)$$

where $\langle \dots \rangle|_\chi$ is evaluated as an emsenble average at the comoving radial distance χ , $J_0(x)$ is the zeroth-order Bessel function, and we have adopted the Limber approximation. It is worth noting that the observed dispersion measures should contain the contributions from the Galaxy as well as near-soure plasma, but our estimator of Eq. (4) is designed to be immune to those contaminations. Hence, we can focus on the correlation between free electrons and galaxies sharing the same large-scale structures.

We use a halo model (Cooray & Sheth 2002) to compute the cross power spectrum of P_{gd} . In the halo model, we can decompose the power spectrum into two terms as

$$P_{\text{gd}}(k) = P_{\text{gd},1h}(k) + P_{\text{gd},2h}(k), \quad (14)$$

where the first term in the right hand side is called the one-halo term arising from two-point correlations inside single halos, while the second one is the two-halo term corresponding to the correlations between different halos. In the following, we specify our model ingredients to compute P_{gd} as well as the three-dimensional average number density of galaxies $\bar{n}_{g,3D}(z)$.

4.1 Halo occupation distribution of 2MASS galaxies

On the modeling of the 2MASS galaxies, we adopt an HOD to relate the galaxy number density with its host-halo counterpart;

$$n_{g,3D}(\mathbf{x}) = \sum_i \left[\langle N_{\text{cen}} | M_i \rangle \delta_D^{(3)}(\mathbf{x} - \mathbf{x}_i) + \langle N_{\text{sat}} | M_i \rangle U_{\text{sat}}(\mathbf{x} - \mathbf{x}_i) \right], \quad (15)$$

where the summation run over all dark-matter halos, \mathbf{x}_i represents the position of the *i*-th halo, $\delta_D^{(3)}(\mathbf{r})$ is the three-dimensional delta function, and $U_{\text{sat}}(\mathbf{r})$ describes the spacial distribution of satellite galaxies in single host halos. In Eq. (15), the terms of $\langle N_{\text{cen}} | M \rangle$ and $\langle N_{\text{sat}} | M \rangle$ are called the halo occupation number, meaning the number of central and satellite galaxies in single host halos with their masses of M , respectively.

For the halo occupation number and the satellite profile of U_{sat} , we use the model as constrained by the power-spectrum analysis in Ando et al. (2018). Those are given by

$$\langle N_{\text{cen}} | M \rangle = \frac{1}{2} \left[1 + \text{erf} \left(\frac{\log M - \log M_{\text{min}}}{\sigma_{\log M}} \right) \right], \quad (16)$$

$$\langle N_{\text{sat}} | M \rangle = \left(\frac{M - M_{\text{min}}}{M_1} \right)^\alpha \Theta(M - M_{\text{min}}), \quad (17)$$

$$U_{\text{sat}}(r) \propto \frac{\Theta(r_{\text{max},g} - r)}{(r/r_{s,g})(1 + r/r_{s,g})^2}, \quad (18)$$

where $\Theta(x)$ is the Heaviside step function. For the halo occupation number, we set the parameters of $\log(M_{\min}/M_{\odot}) = 11.84$, $\sigma_{\log M} = 0.15$, $\log(M_1/M_{\odot}) = 11.98$, and $\alpha = 0.849$, while $r_{s,g} = 0.62 c_{200}^{-1} r_{200}$, and $r_{\max,g} = 6.9 r_{200}$ are adopted in Eq. (18) with c_{200} being the halo concentration parameter. Throughout this paper, we use the model of c_{200} in Duffy et al. (2008). Note that we normalize the satellite profile such that $\int 4\pi r^2 dr U_{\text{sat}}(r) = 1$.

In the end, the average number density of galaxies is then computed as

$$\bar{n}_{g,3D}(z) = \int dM n_h(M, z) [\langle N_{\text{cen}} | M \rangle + \langle N_{\text{sat}} | M \rangle], \quad (19)$$

where $n_h(M, z)$ is the halo mass function (i.e. the number density of halos with M at redshift z). We use the fitting function of $n_h(M, z)$ as developed in Tinker et al. (2008).

4.2 Free electrons around dark matter haloes

In the halo-model framework, we require the electron number density profile around individual halos to compute Eq. (14). For our fiducial choice, we extract spherically symmetric profiles of electron number density around dark matter halos from the IllustrisTNG300 simulation (Springel et al. 2018; Pillepich et al. 2018; Nelson et al. 2018; Marinacci et al. 2018; Naiman et al. 2018). We use the particle snapshot and associated halo catalog at $z = 0$ from the TNG300-1 run. This run employs a box size of $205 h^{-1} \text{Mpc}$ per side and includes 2500^3 gas cells and 2500^3 dark matter particles, enabling us to study free-electron number density across a wide range of halo masses.

For our analysis, we adopt logarithmic halo-mass bins, dividing the range $11 < \log M_{500}/(h^{-1} M_{\odot}) < 14.5$ into 35 bins. Within each mass bin, we compute the average free-electron number density profile as a function of r/r_{500} , where r is the halo-centric radius. Profiles are evaluated in 30 logarithmic bins spanning $0.01 < r/r_{500} < 10$. Even in the most massive bin, we find 14 halos, ensuring that our stacking analysis is robust against statistical fluctuations. To obtain the free-electron abundance from gas cells, we follow the approach in Konietzka et al. (2025). In IllustrisTNG, the electron number density is computed based on ionization equilibrium of primordial gas (Katz et al. 1996). The computed number density is valid for non-star-forming gas cells. However, for star-forming cells, each gas cell is composed of cold and hot interstellar media (Springel & Hernquist 2003), and only the latter contributes to the free electron number density. Here, we simply ignore the star-forming gas cells because the cold interstellar medium accounts for roughly 90% of the total density. This approach provides a lower limit on the electron density profile in the TNG300-1 simulation. However, the prediction already conflicts with our measurements at small scales (see Fig. 4); including star-forming gas cells would only worsen the discrepancy, making the model even less compatible with observations.

Given the tables of the electron number density profile $n_{e,h}(r, M)$, we then compute the halo-model power spectrum of Eq. (14) as (e.g. see van den Bosch et al. 2013 for a similar expression in the context of galaxy-galaxy lensing)

$$P_{\text{gd},1h}(k) = \int dM n_h(M) \tilde{U}_g(k) \tilde{n}_{e,h}(k, M), \quad (20)$$

$$P_{\text{gd},2h}(k) = P_L(k) \left\{ \int dM b_h(M) n_h(M) \tilde{n}_{e,h}(k, M) \right\} \times \left\{ \int dM b_h(M) n_h(M) \tilde{U}_g(k) \right\}, \quad (21)$$

$$\tilde{U}_g(k) = \langle N_{\text{cen}} | M \rangle + \langle N_{\text{sat}} | M \rangle \tilde{U}_{\text{sat}}(k), \quad (22)$$

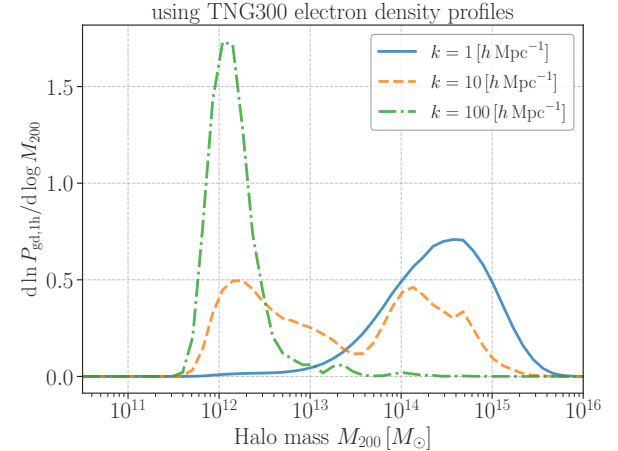


Fig. 3. The derivative of the one-halo cross power spectrum (defined in Eq. 20) with respect to halo masses. In this figure, the blue solid, orange dashed, and green dashed-dotted lines represent the results for three scales of $1, 10$, and $100 h \text{Mpc}^{-1}$, respectively. We here set the redshift to be 0.03 as an effective redshift of the 2MASS galaxies. Alt text: Three line graphs.

where the quantity with tilde represents the Fourier transform of its correspondence, $b_h(M)$ is the linear bias of halos with M , and $P_L(k)$ is the linear power spectrum of cosmic mass density. Throughout this paper, we adopt the halo bias model $b_h(M)$ from Tinker et al. (2010) and use the Boltzmann solver CAMB (Lewis et al. 2000) to compute $P_L(k)$. In Eqs. (20) and (21), the lower and upper limits of the integral are set to $10^{10.5} h^{-1} M_{\odot}$ and $10^{16} h^{-1} M_{\odot}$, respectively. For halo masses outside the range $11 < \log M_{500}/(h^{-1} M_{\odot}) < 14.5$, we assume that the profile shape can be approximated by that of the lowest or highest mass bin, while scaling the amplitude using a logarithmic extrapolation of the gas-to-halo mass relation. Specifically, we compute the (hot) gas mass for a halo of mass M as

$$M_{\text{gas}}(M) = \int_0^{r_{500}} dr 4\pi r^2 n_{e,h}(r, M) m_p \mu_e, \quad (23)$$

where m_p is the proton mass, $\mu_e = (X_p + Y_p/2)^{-1}$ is the mean molecular weight of electrons, X_p and Y_p represent the primordial mass fractions of hydrogen and helium, respectively. In this paper, we set $X_p = 1 - Y_p = 0.76$.

Note that the contributions outside from $11 < \log M_{500}/(h^{-1} M_{\odot}) < 14.5$ minimally affect our halo-model computation at $R \lesssim 0.1 h^{-1} \text{Mpc}$, which is the main focus in this paper. Figure 3 shows the derivatives of the one-halo term (Eq. 20) to the halo mass M at three different scales of $k = 1, 10$ and $100 h \text{Mpc}^{-1}$. At each fourier mode k , we compute the derivative as

$$\partial P_{\text{gd},1h}(k) / \partial M = n_h(M) \tilde{U}_g(k) \tilde{n}_{e,h}(k, M), \quad (24)$$

which is useful to see an effective halo mass in our halo-model predictions. The figure highlights that the cross power spectrum of P_{gd} contains the information of cluster-scale halos at $k \sim 1 \text{Mpc}^{-1}$, while smaller-scale information of P_{gd} can give valuable insights into less massive objects with $M \sim 10^{12-13} M_{\odot}$. The two-halo terms are also found to be subdominant at $R < 1 h^{-1} \text{Mpc}$ in our analysis setup.

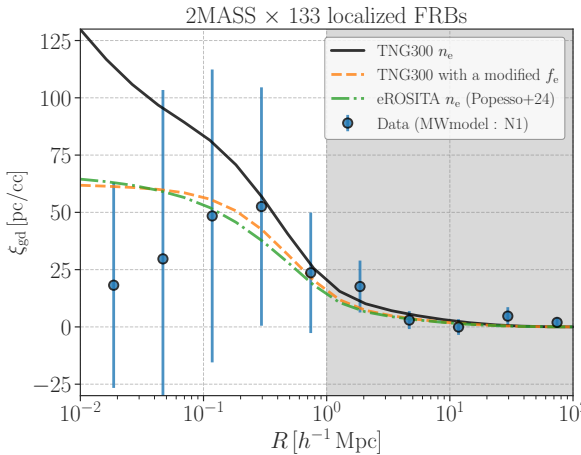


Fig. 4. Comparisons of our measurement with several model predictions. The blue points with error bars show the measured cross correlation functions between the 2MASS galaxies and 133 localized FRBs, while the black solid line stands for our fiducial model prediction based on the electron density profiles extracted from the TNG300-1 simulation. The orange dashed line represents the prediction based on the TNG300 outputs but we reduced the electron abundance f_e in halos with M by a phenomenological function of $\tanh(M_{500}/10^{13.9} M_\odot)$. The green dashed-dotted line is an alternative to the TNG300 electron density profiles with observationally inferred ones in Popesso et al. (2024). Note that the gray region in this figure highlights our covariance estimate of the cross correlation may be underestimated. Alt text: Graphs and data on the comparison with our cross-correlation measurements and theoretical predictions.

5 Results

5.1 Comparison with model predictions

We first compare our measurements of ξ_{gd} with model predictions based on the TNG-300 simulation. For this purpose, we use the data vector based on FRB dispersion measures with the use of N1 template. Figure 4 summarizes the comparison, showcasing that the TNG300-based prediction (the black line in the figure) is incompatible with our measurement at $R \sim 0.01 \text{ Mpc}$. According to the information content discussed in Fig. 3, we speculate this difference can be caused by an overpredicted hot gas mass at group-sized halos in the TNG-300 simulations. To quantify the difference, we simply modify our halo-model predictions by reducing contributions from lower-mass halo as

$$n_{e,h}(r, M) \rightarrow \tanh(M_{500}/M_{\text{cut}}) n_{e,h}(r, M), \quad (25)$$

where M_{cut} is a parameter in this phenomenological model. The orange dashed line in the figure shows the predictions with $M_{\text{cut}} = 10^{13.9} M_\odot$, being in agreement with our measurements.

Another check is also performed with a different functional form in electron density profiles derived in Popesso et al. (2024). The model of Popesso et al. (2024) has been constructed from X-ray stacking analyses for optically-selected galaxy groups in the GAMA survey (Robotham et al. 2011) and X-ray data from eROSITA Science Verification data over the eROSITA Final Equatorial Depth Survey (eFEDS; Brunner et al. 2022). They found the data can be reasonably fitted with an electron density profile as

$$n_{e,P24}(r) = n_0 (r/r_c)^{-\alpha/2} [1 + (r/r_c)^2]^{-3\beta/2 + \alpha/4} \times [1 + (r/r_s)^3]^{-\epsilon/6}, \quad (26)$$

where the parameters of $n_0, \alpha, \beta, \epsilon, r_c$, and r_s are all dependent of

halo masses M . For those parameters, we interpolate the results in Table 1 in Popesso et al. (2024). It is worth noting that Eq. (26) predicts the hot gas mass fraction $M_{\text{gas}}/M \sim 0.1 \Omega_b/\Omega_m$ at $M \sim 10^{13} M_\odot$, while the fraction at the same mass range gets higher by a factor of 2–3 in the TNG model. The green dashed-dotted line in Fig. 4 shows that the model prediction based on Eq. (26) is also consistent with our measurements, necessitating that the hot gas mass at $M \sim 10^{13} M_\odot$ should be of an order of 10% of the global baryon fraction.

5.2 Implication to gas-to-halo mass relations

Using the null detection and the phenomenological model with Eq. (25), we can put a lower limit of M_{cut} as $M_{\text{cut}} > 1 \times 10^{12} M_\odot$ at a 95% confidence level. This is derived by a one-parameter likelihood analysis with the data in the range of $0.01 < R [h^{-1} \text{Mpc}] < 0.2$, where the boost factors are consistent with unity. In practice, we set the limit by solving the equations below;

$$\Delta\chi^2(M_{\text{cut}}) = \chi^2(M_{\text{cut}}) - \min[\chi^2(M_{\text{cut}})] = 4, \quad (27)$$

$$\chi^2(M_{\text{cut}}) = \sum_{ij} \Delta\xi_{\text{gd}}(R_i|M_{\text{cut}}) \text{Cov}_{ij}^{-1} \Delta\xi_{\text{gd}}(R_j|M_{\text{cut}}) \quad (28)$$

$$\Delta\xi_{\text{gd}}(R|M_{\text{cut}}) = \hat{\xi}_{\text{gd}}(R) - \xi_{\text{gd,model}}(R|M_{\text{cut}}), \quad (29)$$

where $\xi_{\text{gd,model}}$ is our halo-model prediction with the modification of Eq. (25) and we find $\min[\chi^2(M_{\text{cut}})] = 1.3$ with 2 degrees of freedom at $M_{\text{cut}} = 4 \times 10^{14} M_\odot$.

Our limit of M_{cut} can be translated into the constraint in the gas-to-halo mass relation at group-mass scales of $M = 10^{12-13} M_\odot$. Figure 5 shows our constraint of the hot-gas mass fraction defined by $f_{\text{gas,hot}} < \tanh(M_{500}/[1 \times 10^{12} M_\odot]) M_{\text{gas}}/M_{500}$ as a function of halo masses. In the figure, the orange filled region stands for our constraint by the galaxy-FRB cross correlation, whereas detailed mass dependence in the upper limit has little meaning. Caution that the hot gas mass from the TNG300 depends on M_{500} , leading that our limit of $f_{\text{gas,hot}}$ exhibits a different dependence from the tanh form. The other filled regions and pink points with error bars show the constraints by different methods in the literature; the cyan filled region has been derived from the stacking analysis of thermal Sunyaev-Zel'dovich (SZ) effect at galaxy groups in the Sloan Digital Sky Survey (Lim et al. 2021); the hatched region comes from multi-wavelength observations of an X-ray-selected sample (Akino et al. 2022); the gray filled region represents the limits inferred from a joint analysis of kinematic SZ effects of massive galaxies and cosmic-shear autocorrelations (Bigwood et al. 2024); the pink points with error bars are the limits from the X-ray analysis in Popesso et al. (2024). We confirm that our limit is in good agreement with those observational results, although the thermal SZ limit relies on virial-temperature assumption and the X-ray analyses may be subject to contaminations from point-source emissions. It is beneficial to mention that our method directly probes electron density profiles at very small scales of $O(0.01) \text{ Mpc}$, whereas the current kinematic SZ analysis can not measure such small-scale signals in a direct way.

Our constraint also allows us to validate existing models of baryonic feedback effects implemented in several numerical simulations. As representative examples, we take the predictions from the FABLE (Henden et al. 2018) and its variant of XFABLE (Bigwood et al. 2025), the FLAMINGO suite (Schaye et al. 2023; Kugel et al. 2023), the BAHAMAS suite (McCarthy et al. 2017), and the SIMBA (Davé et al. 2019). Different colored lines in Fig. 5 represent the predicted gas-to-halo mass relations in those

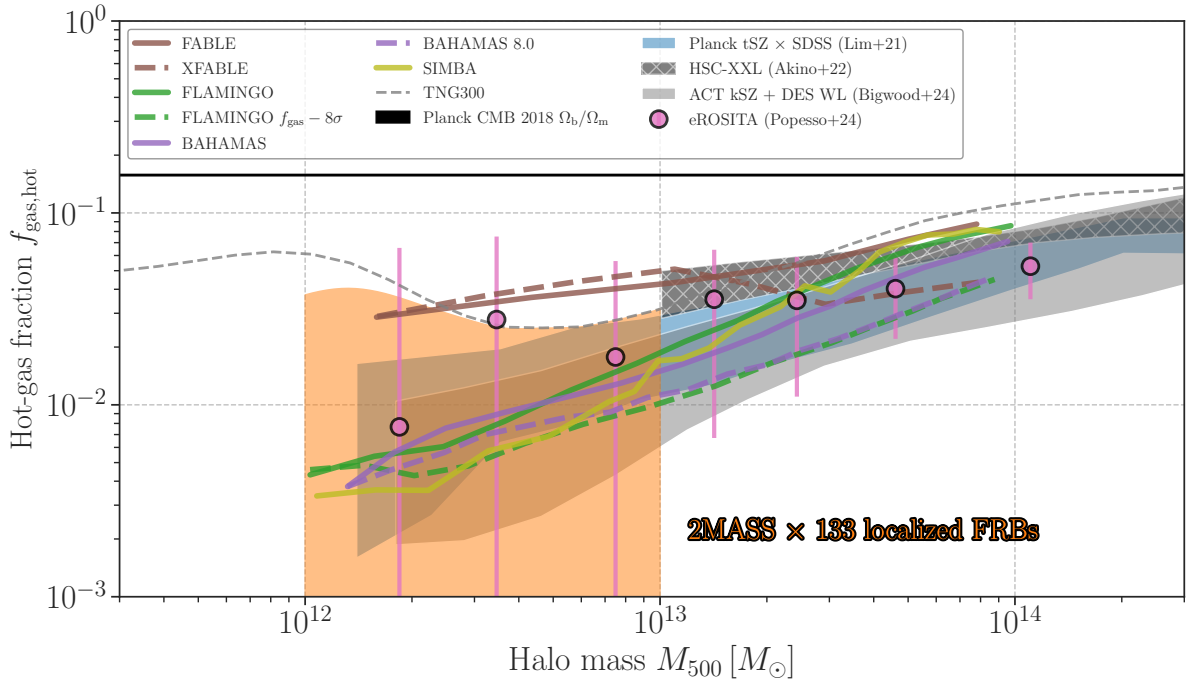


Fig. 5. The limit of gas-to-halo mass relations by our cross correlation measurements along with others. The orange filled region shows our constraint with a 95% confidence level, while the cyan filled, black hatched, gray filled regions and pink points with error bars represent the observational limits based on Lim et al. (2021), Akino et al. (2022), Bigwood et al. (2024), and Popesso et al. (2024), respectively. For reference, we also plot the model predictions based on different hydrodynamical simulations; gray dashed line stands for the TNG300, while brown, green, purple, yellow lines correspond to the predictions for the FABLE and XFABLE suite (Henden et al. 2018; Bigwood et al. 2025), the FLAMINGO suite (Schaye et al. 2023; Kugel et al. 2023), the BAHAMAS suite (McCarthy et al. 2017), and the SIMBA (Davé et al. 2019), respectively. The black solid horizontal line represents the global baryon fraction with the best-fit values inferred from the Planck observation (Planck Collaboration et al. 2020). Alt text: Graphs and data on constraints of the gas-to-halo mass relation.

models, highlighting some strong feedback mechanisms may be required to deplete the hot gas at group scales. More detailed comparisons with simulation-based predictions are highly encouraged and left for future studies. Let us stress that every cosmological hydrodynamical simulation has been calibrated to reproduce the present-day stellar mass function so far, but it is not always consistent with some observational limits on hot gasses. Figure 5 clarifies the need of further additional constraints on gas contents in the universe to improve our understanding of cosmic structure formation.

6 Conclusions

In this paper, we performed a cross-correlation analysis using the 2MASS galaxy catalog and 133 localized Fast Radio Bursts (FRBs). By leveraging redshift information, we measured the real-space correlation function between the foreground galaxy number density and the dispersion measures of background FRBs as a function of comoving separation R . The correlation function $\xi_{\text{gd}}(R)$ was designed to be insensitive to contributions from Galactic dispersion measures and host-galaxy components, enabling us to probe the average free-electron density around 2MASS galaxies at an effective redshift of ~ 0.03 . Our main findings are summarized below:

- Measurements of $\xi_{\text{gd}}(R)$ in the range $0.01 < R [h^{-1}\text{Mpc}] < 1$ are fully consistent with a null detection at about 2σ level. We confirmed that variations in component separation for disper-

sion measures have minimal impact on our results. Furthermore, we found no significant systematics in our background selection, demonstrating the robustness of our estimator for $\xi_{\text{gd}}(R)$.

- We used the IllustrisTNG-300 simulation data to predict $\xi_{\text{gd}}(R)$ within a standard halo-model framework. Our analysis indicates that small-scale measurements of $\xi_{\text{gd}}(R)$ at $0.01\text{--}0.1 h^{-1}\text{Mpc}$ are sensitive to fluctuations in free-electron number density within group-scale halos of mass $10^{12\text{--}13} M_\odot$.
- Our measured $\xi_{\text{gd}}(R)$ at $R \sim 0.01 h^{-1}\text{Mpc}$ is incompatible with the IllustrisTNG-300-based prediction, suggesting an overestimation of hot gas masses in halos of $10^{12\text{--}13} M_\odot$ in the simulation. Introducing a phenomenological cutoff in the gas-to-halo mass relation improves the agreement with our measurements. We also verified that an alternative electron density model inferred from X-ray stacking analyses in Popesso et al. (2024) is consistent with our results.
- Comparing our measurements with the IllustrisTNG-based model allows us to place meaningful constraints on hot gas masses in halos of $10^{12\text{--}13} M_\odot$. We find an upper limit on the hot-gas mass fraction of ~ 0.03 , corresponding to $\sim 10\%$ of the global baryon fraction. This limit is consistent with constraints from the Sunyaev-Zel'dovich effect and X-ray emission measurements around galaxies, while ruling out baryonic feedback scenarios implemented in several hydrodynamical simulation models.

It is important to note that our measurements are based on only $O(100)$ FRBs. Ongoing and future radio surveys, combined with

Table 1. A summary of our cross correlation measurements. We measure the cross correlation ξ_{gd} in units of pc/cc with component separations of observed dispersion measures by adopting four different model templates (denoted as N1, Nbta, Y1, and Ybeta). See Takahashi et al. (2025) for details of the component separations. The error bars are estimated with 40 jackknife sampling of 2MASS galaxies.

$R [h^{-1}\text{Mpc}]$	$\hat{\xi}_{\text{gd}}$ (N1)	$\hat{\xi}_{\text{gd}}$ (Nbta)	$\hat{\xi}_{\text{gd}}$ (Y1)	$\hat{\xi}_{\text{gd}}$ (Ybeta)
0.0186	18.2 ± 44.8	19.2 ± 44.5	19.6 ± 48.4	20.8 ± 47.5
0.0468	29.7 ± 73.7	39.1 ± 83.1	31.8 ± 78.2	41.7 ± 88.3
0.117	48.4 ± 63.9	54.3 ± 71.7	51.4 ± 69.0	57.9 ± 77.6
0.295	52.5 ± 52.0	55.9 ± 56.4	53.1 ± 53.3	56.6 ± 57.9
0.742	23.6 ± 26.2	27.9 ± 31.2	23.3 ± 27.4	27.7 ± 32.7

follow-up observations, will significantly increase the number of localized FRBs. A larger FRB sample will reduce statistical uncertainties and enable detection of cross-correlations between large-scale structures and dispersion measures, providing a powerful tool for mapping hot gas content in the universe. As a conservative choice, we excluded measurements at $R > 1 h^{-1}\text{Mpc}$, but detailed modeling of FRBs and cosmic dispersion measures will allow the generation of synthetic mock FRB datasets and robust evaluation of statistical uncertainties at large R . Furthermore, measurements of cross-correlations across different foreground redshifts and galaxies' properties (e.g. luminosity and colors) can precisely constrain the evolution of hot gas in large-scale structures, offering deeper insights into baryon cycles in the universe.

Acknowledgments

We thank all scientists who made their valuable observational data of FRBs and 2MASS galaxies publicly available. Simulation data used in this paper is kindly provided by The TNG Collaboration: <https://www.tng-project.org/>.

Funding

This research is supported in part by JSPS KAKENHI grant Nos. 20H05855 (RT), 22H00130 (RT and KI), 23H04900 (KI), 23H05430 (KI), 23H01172 (KI), 24H00215 (MS and KO), 24H00221(MS), 25K17380 (KO), 25H01513 (KO), and 25H00662 (KO). MS also aknowledge research supports by JST BOOST, Japan Grant Number JPMJBY24D8. Numerical analyses were [in part] carried out on analysis servers at the Center for Computational Astrophysics, National Astronomical Observatory of Japan.

Data availability

The 2MASS catalogue and the IllustrisTNG-300 simulations are already publicly available. Other data in this article will be shared on a reasonable request to the first author.

Appendix1 Cross-correlation measurements

Table 1 provides numerical values of the cross correlation functions between the 2MASS galaxies and 133 localized FRBs. The covariance matices of individual measurements are given by

$$\text{Cov}_{ij} / \sqrt{\text{Cov}_{ii}\text{Cov}_{jj}} = \begin{pmatrix} 1 & 0.166 & 0.179 & 0.351 & 0.339 \\ 0.166 & 1 & 0.954 & 0.940 & 0.866 \\ 0.179 & 0.954 & 1 & 0.952 & 0.891 \\ 0.351 & 0.940 & 0.952 & 1 & 0.969 \\ 0.339 & 0.866 & 0.891 & 0.969 & 1 \end{pmatrix} \quad (30)$$

for N1,

$$\text{Cov}_{ij} / \sqrt{\text{Cov}_{ii}\text{Cov}_{jj}} = \begin{pmatrix} 1 & 0.174 & 0.186 & 0.350 & 0.345 \\ 0.174 & 1 & 0.962 & 0.943 & 0.869 \\ 0.186 & 0.962 & 1 & 0.958 & 0.895 \\ 0.350 & 0.943 & 0.958 & 1 & 0.972 \\ 0.345 & 0.869 & 0.895 & 0.972 & 1 \end{pmatrix} \quad (31)$$

for Nbta,

$$\text{Cov}_{ij} / \sqrt{\text{Cov}_{ii}\text{Cov}_{jj}} = \begin{pmatrix} 1 & 0.164 & 0.180 & 0.343 & 0.328 \\ 0.164 & 1 & 0.961 & 0.950 & 0.882 \\ 0.180 & 0.961 & 1 & 0.956 & 0.902 \\ 0.343 & 0.950 & 0.956 & 1 & 0.971 \\ 0.328 & 0.882 & 0.902 & 0.971 & 1 \end{pmatrix} \quad (32)$$

for Y1,

$$\text{Cov}_{ij} / \sqrt{\text{Cov}_{ii}\text{Cov}_{jj}} = \begin{pmatrix} 1 & 0.174 & 0.188 & 0.344 & 0.335 \\ 0.174 & 1 & 0.967 & 0.951 & 0.884 \\ 0.188 & 0.967 & 1 & 0.961 & 0.906 \\ 0.344 & 0.951 & 0.961 & 1 & 0.974 \\ 0.335 & 0.884 & 0.906 & 0.974 & 1 \end{pmatrix} \quad (33)$$

for Ybeta, respectively.

References

Akino, D., Eckert, D., Okabe, N., et al. 2022, PASJ, 74, 175
 Amon, A., & Efstathiou, G. 2022, MNRAS, 516, 5355
 Amon, A., Gruen, D., Troxel, M. A., et al. 2022, Phys. Rev. D, 105, 023514
 Ando, S., Benoit-Lévy, A., & Komatsu, E. 2018, MNRAS, 473, 4318
 Aricò, G., Angulo, R. E., Zennaro, M., et al. 2023, A&A, 678, A109
 Asgari, M., Lin, C.-A., Joachimi, B., et al. 2021, A&A, 645, A104
 Bigwood, L., Bourne, M. A., Iršič, V., Amon, A., & Sijacki, D. 2025, MNRAS, 542, 3206
 Bigwood, L., Amon, A., Schneider, A., et al. 2024, MNRAS, 534, 655
 Broxterman, J. C., Simon, P., Porth, L., et al. 2025, A&A, 703, L3
 Brunner, H., Liu, T., Lamer, G., et al. 2022, A&A, 661, A1
 Chawla, P., Kaspi, V. M., Ransom, S. M., et al. 2022, ApJ, 927, 35
 Chen, A., Aricò, G., Huterer, D., et al. 2023, MNRAS, 518, 5340
 Chisari, N. E., Mead, A. J., Joudaki, S., et al. 2019, The Open Journal of Astrophysics, 2, 4
 Cooray, A., & Sheth, R. 2002, Phys. Rep., 372, 1
 Cordes, J. M., & Lazio, T. J. W. 2002, arXiv e-prints, astro
 Cordes, J. M., Wharton, R. S., Spitler, L. G., Chatterjee, S., & Wasserman, I. 2016, arXiv e-prints, arXiv:1605.05890
 Dalal, R., Li, X., Nicola, A., et al. 2023, Phys. Rev. D, 108, 123519
 Davé, R., Anglés-Alcázar, D., Narayanan, D., et al. 2019, MNRAS, 486, 2827
 Dekel, A., & Silk, J. 1986, ApJ, 303, 39
 Duffy, A. R., Schaye, J., Kay, S. T., & Dalla Vecchia, C. 2008, MNRAS, 390, L64
 Eckert, D., Gaspari, M., Gastaldello, F., Le Brun, A. M. C., & O'Sullivan, E. 2021, Universe, 7, 142
 Fabian, A. C. 2012, ARA&A, 50, 455
 Górski, K. M., Hivon, E., Banday, A. J., et al. 2005, ApJ, 622, 759
 Guo, Q., & Lee, K.-G. 2025, MNRAS, 540, 289
 Henden, N. A., Puchwein, E., Shen, S., & Sijacki, D. 2018, MNRAS, 479, 5385
 Hirata, C. M., Mandelbaum, R., Seljak, U., et al. 2004, MNRAS, 353, 529
 Hu, W., & Kravtsov, A. V. 2003, ApJ, 584, 702
 Huang, S., Leauthaud, A., Bradshaw, C., et al. 2022, MNRAS, 515, 4722
 Huchra, J. P., Macri, L. M., Masters, K. L., et al. 2012, ApJS, 199, 26
 Hussaini, M., Connor, L., Konietzka, R. M., et al. 2025, ApJL, 993, L27
 Ioka, K. 2003, ApJL, 598, L79

Jaroszyński, M. 2020, *Acta Astronomica*, 70, 87

Katz, N., Weinberg, D. H., & Hernquist, L. 1996, *ApJS*, 105, 19

Konietzka, R. M., Connor, L., Semenov, V. A., et al. 2025, arXiv e-prints, arXiv:2507.07090

Kovacs, T. O., Mao, S. A., Basu, A., et al. 2024, *A&A*, 690, A47

Kugel, R., Schaye, J., Schaller, M., et al. 2023, *MNRAS*, 526, 6103

Lavaux, G., & Hudson, M. J. 2011, *MNRAS*, 416, 2840

Leung, C., Borrow, J., Masui, K. W., et al. 2025, arXiv e-prints, arXiv:2509.19514

Lewis, A., Challinor, A., & Lasenby, A. 2000, *ApJ*, 538, 473

Li, X., Zhang, T., Sugiyama, S., et al. 2023, *Phys. Rev. D*, 108, 123518

Lim, S. H., Barnes, D., Vogelsberger, M., et al. 2021, *MNRAS*, 504, 5131

Mandelbaum, R. 2015, in IAU Symposium, Vol. 311, Galaxy Masses as Constraints of Formation Models, ed. M. Cappellari & S. Courteau, 86–95

Mandelbaum, R., Hirata, C. M., Seljak, U., et al. 2005, *MNRAS*, 361, 1287

Marinacci, F., Vogelsberger, M., Pakmor, R., et al. 2018, *MNRAS*, 480, 5113

McCarthy, I. G., Schaye, J., Bird, S., & Le Brun, A. M. C. 2017, *MNRAS*, 465, 2936

Medlock, I., Nagai, D., Anglés-Alcázar, D., & Gebhardt, M. 2025, *ApJ*, 983, 46

Medlock, I., Nagai, D., Singh, P., et al. 2024, *ApJ*, 967, 32

Merryfield, M., Tendulkar, S. P., Shin, K., et al. 2023, *AJ*, 165, 152

Mo, J.-F., Zhu, W., Wang, Y., Tang, L., & Feng, L.-L. 2023, *MNRAS*, 518, 539

Naiman, J. P., Pillepich, A., Springel, V., et al. 2018, *MNRAS*, 477, 1206

Nelson, D., Pillepich, A., Springel, V., et al. 2018, *MNRAS*, 475, 624

Nicola, A., Villaescusa-Navarro, F., Spergel, D. N., et al. 2022, *Journal of Cosmology and Astroparticle Physics*, 2022, 046

Norberg, P., Baugh, C. M., Gaztañaga, E., & Croton, D. J. 2009, *MNRAS*, 396, 19

Ocker, S. K., Cordes, J. M., Chatterjee, S., & Gorsuch, M. R. 2022, *ApJ*, 934, 71

Petroff, E., Hessels, J. W. T., & Lorimer, D. R. 2019, *A&AR*, 27, 4

Pillepich, A., Nelson, D., Hernquist, L., et al. 2018, *MNRAS*, 475, 648

Planck Collaboration, Aghanim, N., Akrami, Y., et al. 2020, *A&A*, 641, A6

Popesso, P., Biviano, A., Marini, I., et al. 2024, arXiv e-prints, arXiv:2411.16555

Reischke, R., & Hagstotz, S. 2025, arXiv e-prints, arXiv:2507.17742

Reischke, R., Kovač, M., Nicola, A., Hagstotz, S., & Schneider, A. 2025, *The Open Journal of Astrophysics*, 8, 127

Reischke, R., Neumann, D., Bertmann, K. A., Hagstotz, S., & Hildebrandt, H. 2023, arXiv e-prints, arXiv:2309.09766

Robotham, A. S. G., Norberg, P., Driver, S. P., et al. 2011, *MNRAS*, 416, 2640

Schaye, J., Kugel, R., Schaller, M., et al. 2023, *MNRAS*, 526, 4978

Secco, L. F., Samuroff, S., Krause, E., et al. 2022, *Phys. Rev. D*, 105, 023515

Seebeck, J., Ravi, V., Connor, L., et al. 2021, arXiv e-prints, arXiv:2112.07639

Sharma, K., Krause, E., Ravi, V., et al. 2025a, arXiv e-prints, arXiv:2509.05866

—. 2025b, *ApJ*, 989, 81

Shirasaki, M., Kashiyama, K., & Yoshida, N. 2017a, *Phys. Rev. D*, 95, 083012

Shirasaki, M., Takada, M., Miyatake, H., et al. 2017b, *MNRAS*, 470, 3476

Shirasaki, M., Takahashi, R., Osato, K., & Ioka, K. 2022, *MNRAS*, 512, 1730

Shivraj Patil, S., Main, R. A., Fonseca, E., et al. 2025, arXiv e-prints, arXiv:2509.06721

Singh, S., Mandelbaum, R., Seljak, U., Slosar, A., & Vazquez Gonzalez, J. 2017, *MNRAS*, 471, 3827

Skrutskie, M. F., Cutri, R. M., Stiening, R., et al. 2006, *AJ*, 131, 1163

Springel, V., & Hernquist, L. 2003, *MNRAS*, 339, 289

Springel, V., Pakmor, R., Pillepich, A., et al. 2018, *MNRAS*, 475, 676

Takahashi, R., Ioka, K., Mori, A., & Funahashi, K. 2021, *MNRAS*, 502, 2615

Takahashi, R., Ioka, K., Shirasaki, M., & Osato, K. 2025, arXiv e-prints, arXiv:2511.02155

Terasawa, R., Li, X., Takada, M., et al. 2025, *Phys. Rev. D*, 111, 063509

Theis, A., Hagstotz, S., Reischke, R., & Weller, J. 2024, arXiv e-prints, arXiv:2403.08611

Tinker, J., Kravtsov, A. V., Klypin, A., et al. 2008, *ApJ*, 688, 709

Tinker, J. L., Robertson, B. E., Kravtsov, A. V., et al. 2010, *ApJ*, 724, 878

Umetsu, K. 2020, *A&AR*, 28, 7

Valentini, M., & Dolag, K. 2025, arXiv e-prints, arXiv:2502.06954

van den Bosch, F. C., More, S., Cacciato, M., Mo, H., & Yang, X. 2013, *MNRAS*, 430, 725

Vedantham, H. K., & Phinney, E. S. 2019, *MNRAS*, 483, 971

Wang, H., Masui, K., Andrew, S., et al. 2025, arXiv e-prints, arXiv:2506.08932

Yamasaki, S., & Totani, T. 2020, *ApJ*, 888, 105

Yao, J. M., Manchester, R. N., & Wang, N. 2017, *ApJ*, 835, 29

Zhang, B. 2023, *Reviews of Modern Physics*, 95, 035005

Zhang, G. Q., Yu, H., He, J. H., & Wang, F. Y. 2020, *ApJ*, 900, 170

Zhang, Z. J., Nagamine, K., Oku, Y., et al. 2025, *ApJ*, 993, 162

Zhou, B., Li, X., Wang, T., Fan, Y.-Z., & Wei, D.-M. 2014, *Phys. Rev. D*, 89, 107303